

Katja Freitag · Alan P. Boyle · Eric Nelson
Murray Hitzman · James Churchill
Magda Lopez-Pedrosa

The use of electron backscatter diffraction and orientation contrast imaging as tools for sulphide textural studies: example from the Greens Creek deposit (Alaska)

Received: 21 March 2003 / Accepted: 5 August 2003 / Published online: 12 September 2003
© Springer-Verlag 2003

Abstract The Greens Creek polymetallic massive sulphide deposit is hosted in a typical polyphase deformed lower greenschist facies orogenic setting. The structure of the host rocks is well constrained, exhibiting a series of three superimposed ductile deformations followed by two brittle episodes. The ore is found both in fold hinges where early-formed depositional features are preserved and in fold limbs where primary features are typically strongly modified or obliterated. Samples from both settings have been investigated using electron backscatter diffraction (EBSD) coupled with foreshoulder orientation contrast (OC) imaging in order to observe the effects of deformation and lower greenschist facies metamorphism on pyrite. Results suggest that colloform pyrite may preserve information relevant to palaeoenvironment, that apparently simple textures are generally more complex, and that pyrite can deform plastically by dislocation glide and creep processes at lower temperatures and/or strain rates than generally accepted. This analysis indicates that EBSD and OC imaging provide powerful tools for observing textural relationships in pyrite that are not shown by more traditional methods. They should become routine tools for pyrite texture analysis.

Keywords Electron backscatter diffraction · Textural imaging · Sulphide textures · Massive sulphide deposits

Introduction

Many economically important sulphide ore deposits have been deformed and metamorphosed, and an understanding of this part of their history is important for their successful exploitation: metamorphism typically alters primary textures, differentially mobilises phases and changes trace element compositions of ore and gangue minerals (e.g. Marshall and Gilligan 1987; Castroviejo 1990; Gaspar and Pinto 1991; Brown and McClay 1993; Xu 1996). Pyrite itself is not typically of economic importance, but it is of geological importance in deformed and metamorphosed sulphide ore deposits because its refractory nature means it has much potential for recording significant parts of the deformation and metamorphic history (Craig and Vokes 1993). Classic studies of pyrite deformation and recrystallisation have relied on: (1) petrographic interpretation of polished specimens in reflected light or in the scanning electron microscope using backscatter electron imaging and/or X-ray chemical mapping (e.g. Castroviejo 1990; Brown and McClay 1993; Craig and Vokes 1993; Craig et al. 1998); (2) transmission electron microscopy (TEM) studies (e.g. Graf et al. 1981; Levade et al. 1982); and (3) experimental deformation and neutron diffraction studies (e.g. Cox et al. 1981; Siemes et al. 1993).

More recently, with the advent of scanning electron microscope (SEM)-based electron backscatter diffraction (EBSD) facilities for the study of geological materials, Boyle et al. (1998) and Prior et al. (1999) have shown that pervasive lattice-scale dislocation glide deformations can be resolved in individual pyrite grains deformed under upper greenschist to lower amphibolite facies conditions. We now extend this approach into lower grade metamorphic conditions by presenting results from the Greens Creek polymetallic sulphide deposit (Fig. 1).

Editorial handling: D. Lentz

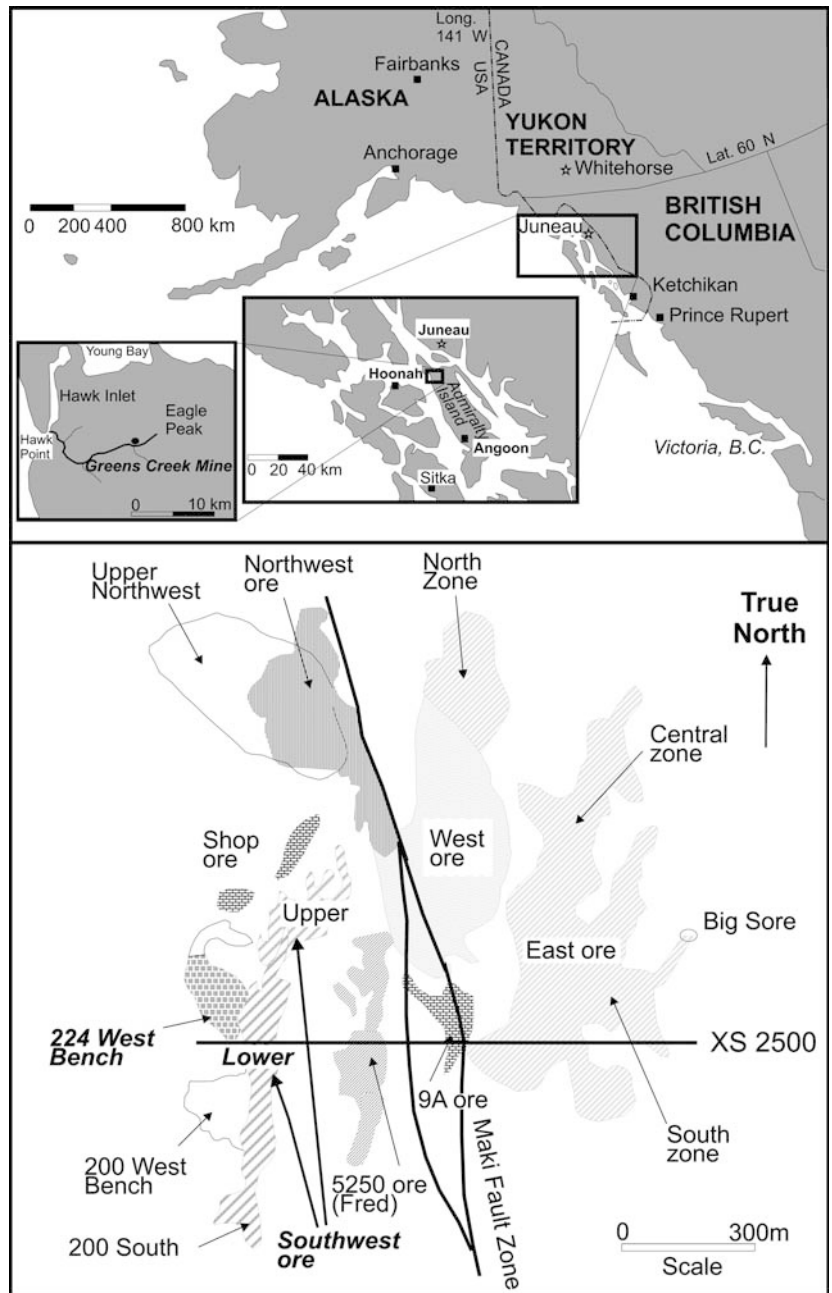
K. Freitag · M. Lopez-Pedrosa
Private Bag X1013, Suite 14, 1390
Phalaborwa, South Africa

A. P. Boyle (✉)
Department of Earth Sciences,
University of Liverpool,
Liverpool, L69 3GP, UK
E-mail: apboyle@liverpool.ac.uk

E. Nelson · M. Hitzman
Department of Geology and Geological Engineering,
Colorado School of Mines,
Golden, Colorado 80401, USA

J. Churchill
Robertson Research International Ltd.,
Llandudno, North Wales, LL30 1SA, UK

Fig. 1 Location and distribution of main ore bodies of the Greens Creek mine area. The Lower Southwest and 224 West Bench ore bodies are highlighted. *Line XS 2500* is the line of section for Fig. 2



Geological setting

The Greens Creek deposit is a Triassic-age, polymetallic Zn-Pb-Ag-Sb-As-Hg-Mo-Tl-(Cu-Au) massive sulphide deposit formed in a low-temperature, shallow-water ore-forming environment in an evolving intra-arc rift (Taylor et al. 1999, 2000; Freitag 2000). The ores are hosted by a discontinuously exposed, 600-km-long belt of rocks comprising a 200- to 800-m-thick rift-fill sedimentary sequence intercalated with bimodal volcanic rocks and intruded by mafic-ultramafic dikes and sills (Taylor et al. 2000). The deposit has undergone at least three stages of folding followed by two brittle deformation events. The folding events have locally overturned parts of the deposit

and largely obliterated original sulphide textures; especially on highly strained fold limbs. Pumpellyite-bearing assemblages in the volcanics indicate that associated peak thermal metamorphism was at about 325 °C and 2–4.8 kbar (Himmelberg et al. 1994, 1995). The deposit thus provides an excellent study area for investigating relatively low-temperature recrystallisation and deformation of pyrite. In particular, sampling both from fold hinges and limbs allows documentation of the microstructural development of pyrite textures from primary colloform and spongy textures through to completely recrystallised textures. The investigated samples are from the Lower Southwest and neighbouring West Bench ore bodies of the Greens Creek deposit (Figs. 1 and 2).

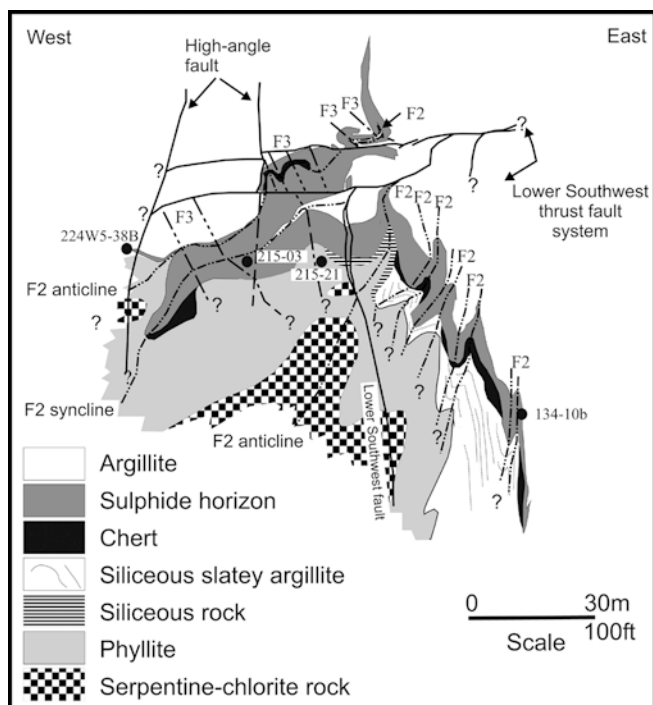
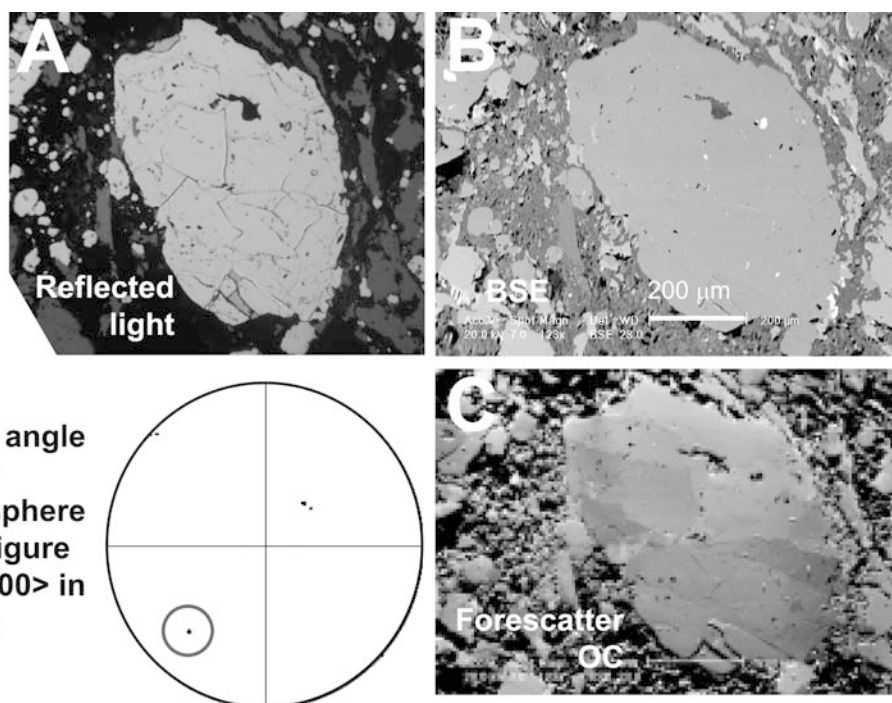


Fig. 2 Geological cross section of Greens Creek deposits showing locations of samples discussed in this article. Line of section is XS 2500 in Fig. 1. The *lithological key* is ordered in structural sequence from the core of the major F₂ anticline to the argillite above the main sulphide ore horizon

Methods

Four specimens were chosen for detailed study on the basis of structural setting (fold limbs and hinges) and standard reflected light examination to locate the best examples of primary colloform

Fig. 3 Plane-polarised reflected light (A), BSE (B) and forescatter OC (C) images of the same pyrite grain. Crystallographic orientation variation is summarised as an upper hemisphere $\langle 100 \rangle$ pole figure. Collected using Philips XL30 SEM system



and secondary deformation/recrystallisation textures. Advanced scanning electron microscopy (SEM) utilising electron backscatter diffraction (EBSD) was used. Early work used a user-driven Philips XL30 SEM fitted with a TexSEM system for collection of EBSD patterns (EBSP) and Channel+ v3 software from HKL Software for interpretation of EBSPs. Some later studies used a fully automated CamScan X500 Crystal Probe SEM coupled with Channel+ v5.0 software. See Prior et al. (1996) and Prior et al. (1999) for details of the Philips system and Prior et al. (2002) for details of the CamScan system.

Both systems have the specimen surface tilted at 20° to the electron beam to facilitate EBSD and the collection of an EBSP on a phosphor screen. Positioning of a solid-state detector forward of the specimen to collect electrons scattered by diffraction forward of the specimen allows generation of an orientation contrast image (forescatter OC image), which differs markedly from the more familiar backscatter electron (BSE) image produced from a solid-state detector positioned at a high angle to the specimen surface. Figure 3 compares a standard reflected light image of an ovoid pyrite grain from Greens Creek with a standard BSE image and a forescatter OC image. The reflected light image indicates the presence of brittle fractures, which do not show up well in the BSE image. Both these images suggest internal homogeneity in the domains between the fractures. In comparison, the forescatter OC image indicates there are band-like domains of different crystallographic orientation between the fractures (Fig. 3). EBSD provides full quantitative crystallographic orientation of each domain. Results for the pyrite grain are summarised as a pole figure of $\langle 100 \rangle$ directions in Fig. 3. Note that one $\langle 100 \rangle$ direction (circled) forms a cluster, while the other two directions lie slightly spread out on a great circle. This indicates the pyrite deformed by slight lattice rotation about the circled $\langle 100 \rangle$ direction in Fig. 3.

EBSD work completed using the Philips XL30 system involved collection of a forescatter OC image followed by EBSD analysis of user-selected points in the image. Spatial resolution was limited to around 1 μm. Crystallographic-orientation resolution was always better than ±1°. User-defined selection of points, coupled with user-driven interpretation software, typically results in an average of one analytical point per minute.

The CamScan X500 was used in automated mode. XY grid areas were identified and the system was then instructed to complete a set of analyses automatically at a regular grid spacing

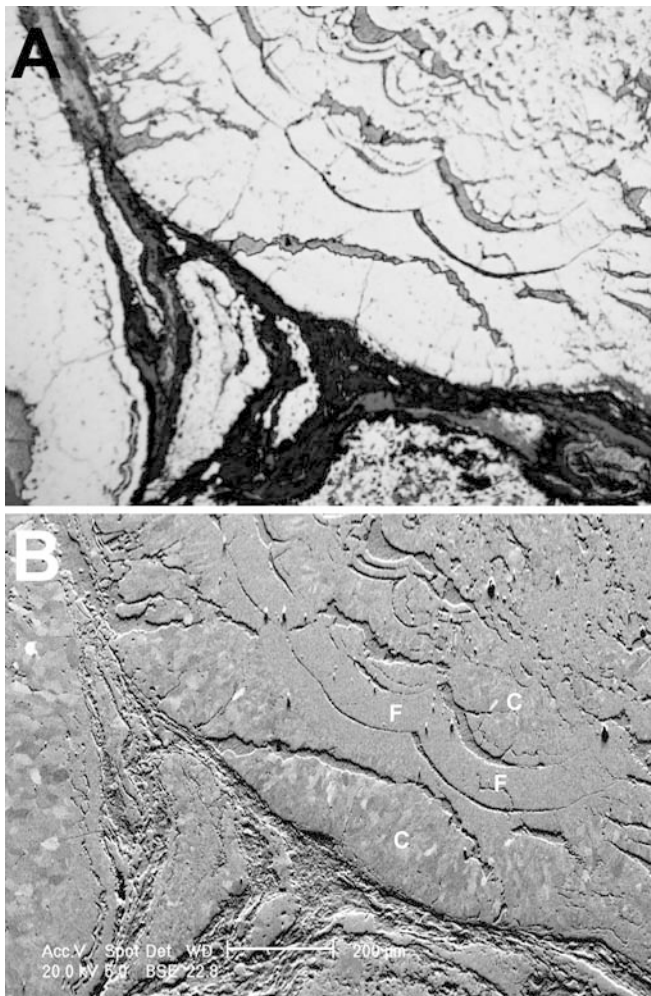


Fig. 4 Plane-polarised reflected light (A) and forescatter OC (B) images of colloform pyrite from specimen 215-03. Layers of pyrite are separated by galena seams, which show up with negative relief in the forescatter OC image due to the very soft nature of galena. Labels C and F refer to coarse- and fine-grained layers, respectively. Collected using Philips XL30 SEM system

(typically 1–10 μm depending on the scale of domains seen in the forescatter OC image). Spatial resolution is better than 1 μm , and crystallographic resolution similar. Each analysis point typically takes less than 1 s, allowing collection of huge amounts of data in a relatively short time, often unattended overnight.

Detailed textural studies

Four specimens were studied in order to document the microstructural development of pyrite textures from primary colloform and spongy textures to thoroughly recrystallised textures.

Specimen 215-03 colloform pyrite

One of the least deformed examples of massive ore from Greens Creek is sample 215-03 from the hinge of a major F_2 fold (Fig. 2). Abundant well-formed colloform pyrite

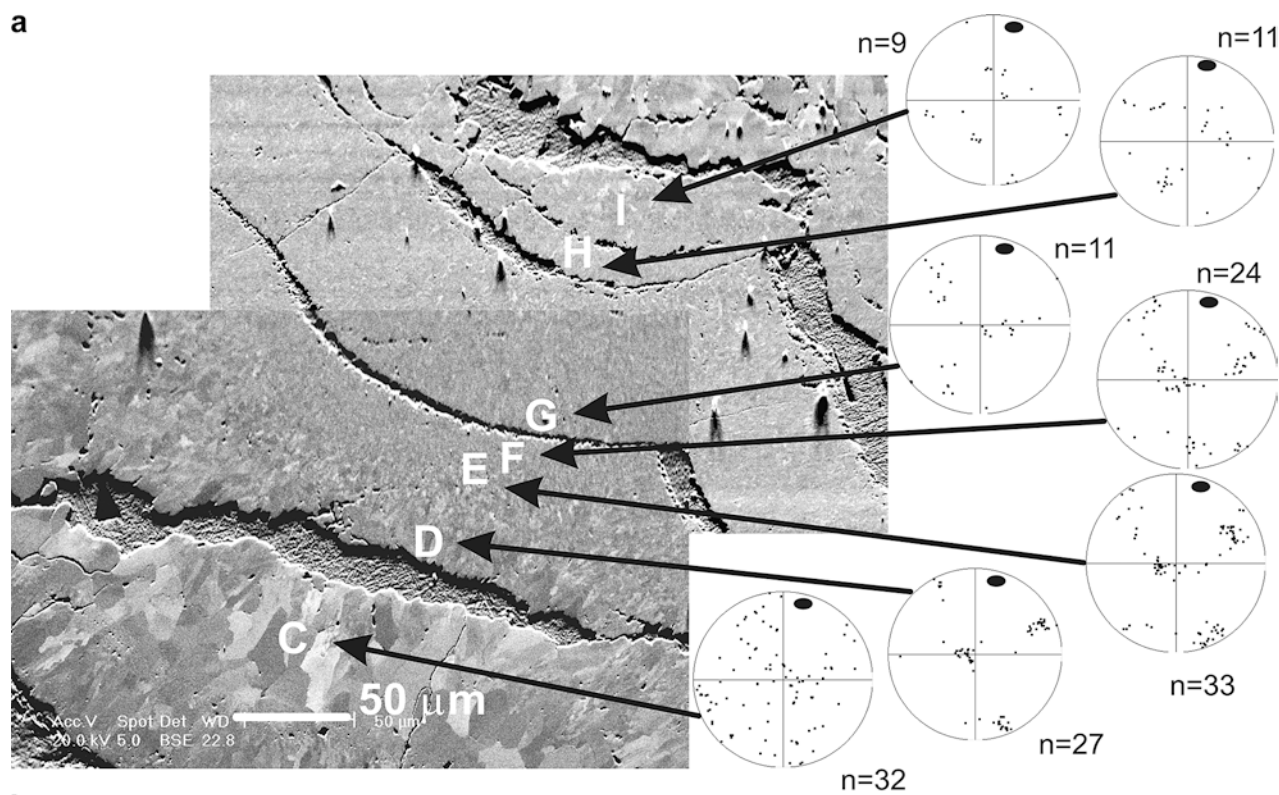
Fig. 5 a Detail of colloform pyrite in Fig. 4 together with manually collected EBSD results plotted as upper hemisphere $\langle 100 \rangle$ pole figures for seven textural domains labelled C–I. Black ellipse on pole figures defines a $\langle 110 \rangle$ direction about which many of the EBSD data are distributed. Collected using Philips XL30 SEM system. **b** Detail of second colloform pyrite in specimen 215-03. EBSD data collected automatically on a micron-spaced grid basis using a CamScan X500 Crystal probe SEM, and plotted as upper hemisphere $\langle 100 \rangle$ pole figures. Small pole figure summaries $\langle 110 \rangle$ orientations for the outermost coarser-grained layer

textures are preserved. Figure 4 compares colloform pyrite development as seen in reflected light and forescatter OC images. Thin seams of galena locally separate concentric colloform layers. Much of the pyrite is very fine grained, typically less than 3 μm , but there are some well-developed layers of coarse radiating pyrite, especially near the margins of colloforms, where individual pyrite crystallites are up to 50 μm in length and 10 μm across. The textures imply that recrystallisation occurred, although the variable grey tones in the OC image of the coarse radiating layers suggest variable crystallographic orientations.

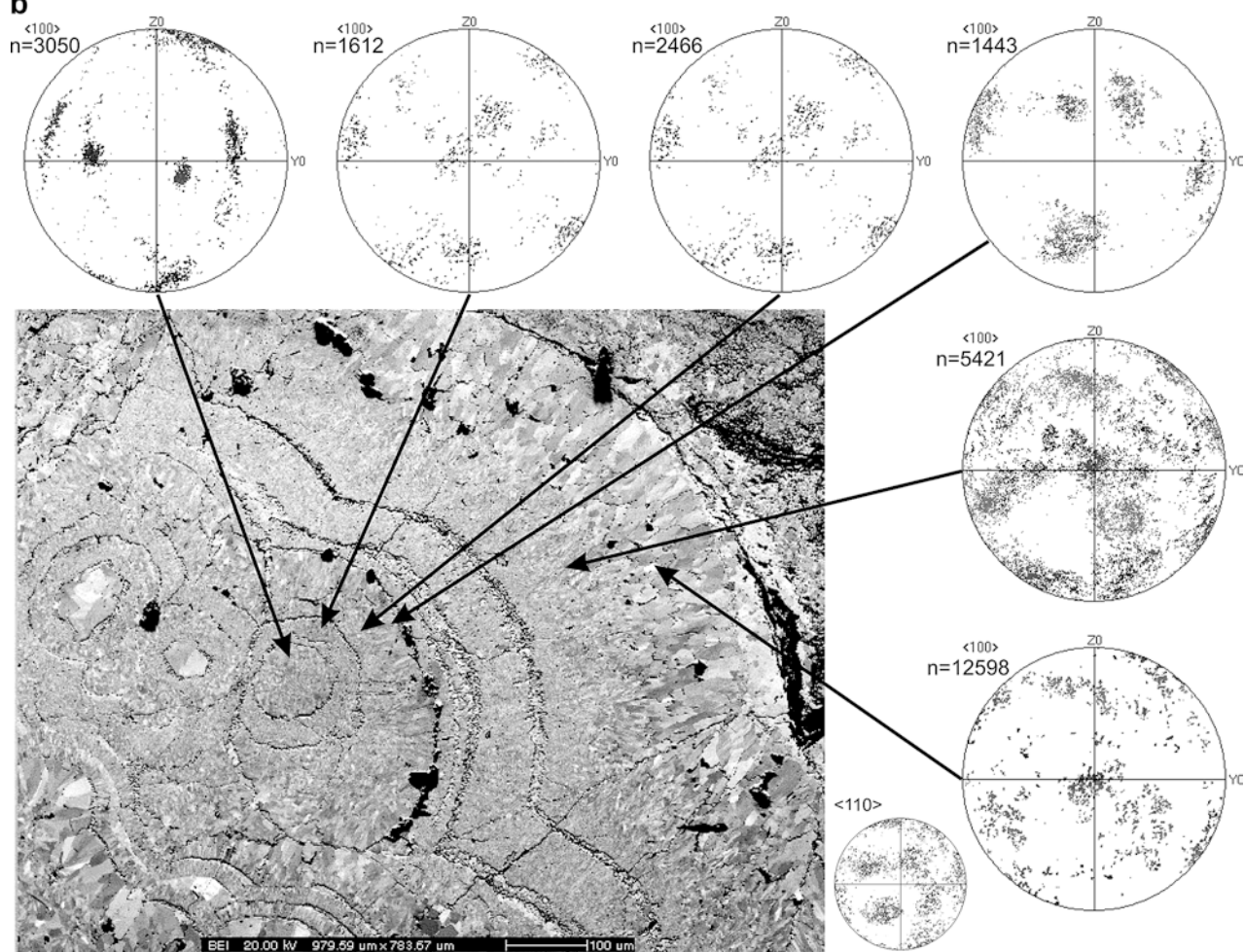
Detailed EBSD analysis across seven distinct textural zones (labelled C through I in Fig. 5a) provides some unusual crystallographic characteristics. From zone I to zone D (Fig. 5a), pyrite microcrysts become increasingly similar in their crystallographic preferred orientation (CPO) as indicated by the increasing clustering of $\langle 100 \rangle$ directions on the pole figures. This progressive change is unaffected by crossing over three galena seams in the colloform texture. However, on crossing over the fourth galena seam into domain C (Fig. 5a) there is an abrupt change in $\langle 100 \rangle$ CPO of the pyrite microcrysts. Although the pyrite here is the coarsest grained, it also has the least well-developed $\langle 100 \rangle$ CPO. However, further investigation of the EBSD data suggests that the scattering of $\langle 100 \rangle$ directions in some domains is systematic about a $\langle 110 \rangle$ direction (indicated by the black ellipse in the pole figures in Fig. 5a). It would thus seem that pyrite orientation switches between a more or less single $\langle 100 \rangle$ set of orientations and a set of orientations best described as a rotation about a single $\langle 110 \rangle$ direction. The former tend to be finer grained, and the latter coarser grained. Two principal factors are likely to affect the CPO of the pyrite microcrysts: (1) orientations inherited from the primary depositional processes responsible for producing the original colloform texture; and (2) orientations produced by subsequent recrystallisation resulting from metamorphism and/or deformation.

It is difficult to conceive a process for the second option. The colloform layers appear generally undeformed, and in the absence of deformation why should recrystallisation produce preferred orientations? In addition, the progressive increase in $\langle 100 \rangle$ CPO followed by a coarser layer with a rotation about $\langle 110 \rangle$ CPO is difficult to reconcile with recrystallisation during deformation. Boyle et al. (1998) have suggested that rotations about $\langle 100 \rangle$ are much more common results

a



b



of pyrite deformation than rotations about $\langle 110 \rangle$, and the latter arise from special textural situations where a pyrite is deformed by severe indentation by the edge of another pyrite grain. The absence of obvious deformation precludes this mechanism. Recrystallisation during recovery can produce changes in grain size, but does not typically produce a CPO radically different from the precursor CPO in the absence of significant shearing deformation to drive grain/subgrain rotation. If the grain coarsening in some layers is due to recovery, then the CPO is likely to be inherited from the precursor.

If the observed CPOs are inherited from original depositional processes, then these processes must have initially created increasing $\langle 100 \rangle$ crystallographic ordering of pyrite followed by a lower level of ordering about a single $\langle 110 \rangle$ direction. A second colloform growth from the same sample was investigated using an automated CamScan X500 Crystal Probe SEM (Fig. 5b). The resulting pole figures, keyed into texturally distinct colloform layers, show a similar sequence of improving $\langle 100 \rangle$ CPO followed by a coarser rim with a rotation about a single $\langle 110 \rangle$ CPO. The small inset pole figure in Fig. 5b summarises $\langle 110 \rangle$ directions for the outermost coarse-grained layer, and clearly identifies a cluster of $\langle 110 \rangle$ direction in the bottom left quadrant of the pole figure, about which the other $\langle 110 \rangle$ directions are dispersed.

A comparison of these results with previous studies of framboidal pyrite is potentially revealing. Framboidal pyrite, as the name suggests, comprises raspberry-shaped aggregates of pyrite microcrysts. Wilkin et al. (1996) noted that framboidal diameters (D) and microcryst diameters (d) are more restricted in size range and generally smaller when formed under anoxic conditions than under oxic/dysoxic conditions. They reported mean framboid microcryst diameters (d) of $5.0 \pm 1.7 \mu\text{m}$ for modern anoxic environments, but larger mean d of $7.7 \pm 4.1 \mu\text{m}$ for oxic and dysoxic environments. More importantly, they noted that D/d ratios are generally lower for framboids formed under anoxic conditions, suggesting that D/d is a palaeoenvironmental indicator. On the basis of crystal size distribution theory, they argued that the primary control was residence time near the oxic–anoxic boundary, with framboid growth times being shorter in euxinic environments than in oxic ones.

A later study by Ohfuji and Akai (2002) reported variation in the packing of pyrite microcrysts inside framboidal pyrites in which the pyrite microcrysts making up the framboid may be either randomly packed or arranged in a regular pattern, i.e. with strong CPO. Ohfuji et al. (2002) found a correlation between the degree of microcryst ordering and D/d for the framboids. The ordered framboids have high D/d and the disordered ones lower D/d, leading Ohfuji et al. (2002) to suggest that ordered framboid microcrysts reflect higher relative pyrite supersaturations nearer to the SO_4^{2-} - $^{\text{I}}\text{S}(-\text{II})$ redox boundary, whereas disordered framboid microcrysts reflect more reducing environments. These works indicate some redox envi-

ronmental control on microcryst CPO in framboidal pyrite.

The colloform structures described here differ from framboids in their mode of origin, the layered form indicating a sequence of nucleation and growth periods rather than the single growth period argued for framboids. However, the variations in microcryst size and CPO provide a potential parallel. The layers with larger microcrysts, lower D/d, are relatively disordered with respect to $\langle 100 \rangle$: characteristics of anoxic conditions in framboidal pyrite. The layers with smaller microcrysts, higher D/d, are better ordered with respect to $\langle 100 \rangle$: characteristics of oxic conditions in framboidal pyrite. Colloform pyrite may have potential for recording changing redox conditions with time. It may also be the case that framboids described as having disordered microcrysts might just have a lower level of ordering related to a rotation about $\langle 110 \rangle$. Further EBSD study of a range of colloform pyrites and framboids is required to develop this idea further.

Specimen 134-10b spongy pyrite

A micro-textural investigation of spongy pyrite was undertaken using sample 134-10b collected from the limb of a major F_2 fold, but adjacent to a parasitic tight F_2 anticline (Fig. 3). An OC image of a spongy pyrite aggregate with a millimetre-scale, slightly flattened square-shaped boundary to the aggregate is shown in Fig. 6A. An OC image (Fig. 6B) of the margin of the spongy pyrite shows that it comprises abundant pore space and weakly developed subgrains that are typically less than $5 \mu\text{m}$ in size. The pole figure indicates that there is uniform or random CPO for pyrite grains within the spongy pyrite.

The peculiar aspect of these images is that the small pyrite grains are randomly oriented, but in aggregate they produce a millimetre-scale square outline. It is common during metamorphism and deformation for larger grains of a mineral to develop an aggregate of subgrains by dynamic recrystallisation. However, it is not common for such a process to produce this degree of subgrain misorientation and still retain the original shape of the host, particularly at lower greenschist facies conditions where pyrite would be expected to behave in a brittle manner. It also seems unlikely that randomly oriented micron-scale grains should aggregate together at the millimetre scale to produce a square outline, though perhaps this is an arrested stage in a mechanism by which larger pyrite grains may be formed from aggregates of smaller pyrite grains. Spiess et al. (2001) and Prior et al. (2002) have proposed such a mechanism (albeit at higher temperature) for potential development of large garnet porphyroblasts whereby closely nucleated small garnets with random CPO grow, coalesce and then adjust their crystallographic orientations by physical rotation driven by boundary energy to form a larger garnet porphyroblast. Further study is required in this area also.

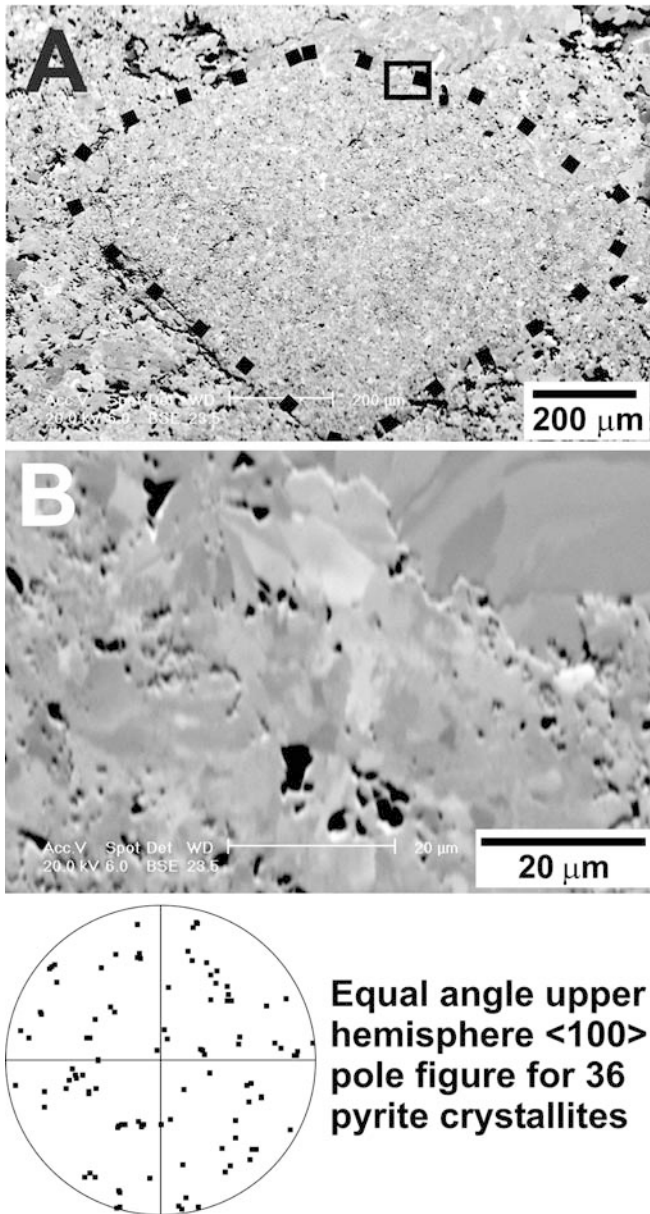


Fig. 6 Orientation contrast images of millimeter-scale spongy pyrite domain with a flattened “square” outline (A) and higher magnification detail (B) in specimen 134-10b. Upper hemisphere $\langle 100 \rangle$ pole figures indicate that individual micron-scale pyrite crystals are randomly oriented. Dotted line highlights margin of “flattened-square”-shape aggregate. Collected using Philips XL30 SEM system

Specimen 215-21 euhedral faceted pyrite with spongy core

Sample 215-21 is from the altered and strongly deformed phyllitic footwall of the massive sulphide body (Fig. 2). Pyrite grains are disseminated, ranging in size from microns up to a millimetre. The larger pyrites tend to have faceted outlines, are wrapped by the phyllitic foliation and have well-developed quartz-bearing pressure shadows. The reflected light and transmitted light textures suggest that the pyrite predates at least some of the

penetrative matrix deformation, but has recrystallised after deformation to develop a faceted outline. The larger pyrites have spongy-looking cores; Fig. 7 showing a typical example in reflected light and OC image. The OC image reveals the spongy core to comprise relatively small grey-scale domains surrounded by a rim of larger grey-scale domains. In the core there is a weakly defined shape preferred orientation (SPO) running from top left to bottom right, subparallel to the enclosing phyllitic matrix cleavage. Conversely, the rim grey-scale domains have a blocky appearance and no SPO.

EBSD indicates that the core area has a strong single CPO (Fig. 7, pole figure *vii*). The three $\langle 100 \rangle$ axes have orientations consistent with the SPO being parallel to two of them and normal to the other, suggesting that the SPO relates directly to a $\{100\}$ plane in pyrite. The same CPO is present in the blocky rim pyrite, but other orientations are present too (Fig. 7 pole figure *x* summarising all blocky rim pyrite). Domains *iii*, *vi* and *viii* have single CPOs similar to the core region. Domains *v* and *ix* have different CPOs. Domains *i*, *ii* and *iv* show elements of the core CPO, but with some dispersion of crystallographic orientations. Overall, two $\langle 100 \rangle$ CPOs dominate in the rim, indicated by three squares and three circles in pole figure *x* in Fig. 7. The circled CPO is restricted to domains *v* and *ix*, suggesting that this corner of the pyrite is a separate grain intergrown with the main pyrite grain. Reflected light observation suggests that domain *i* is a separate grain, though EBSD shows it does not contain a distinct CPO.

The spongy core is clearly distinct from the spongy pyrite discussed in specimen 134-10b, having a strong CPO rather than a random one. It is possible that the CPO may be primary, as discussed for the colloform-bearing sample 215-03. However, given the context of the host phyllite it would seem more likely that early-formed pyrite was deformed during matrix deformation of the host phyllite to develop a subgrain aggregate. Boyle et al. (1998) have described development of a checker-board texture in pyrite deformed at upper greenschist to lower amphibolite facies conditions whereby dislocation glide takes place in multiple $\{100\}$ planes, giving rise to a CPO similar to that in Fig. 7 pole figure *vii*. Depending on relative dominance of a particular glide plane an SPO can be developed. If the spongy cores have developed by dislocation glide parallel to $\{100\}$ pyrite planes, then two things arise with reference to the pyrite deformation mechanisms map (Fig. 8) of McClay and Ellis (1983). The matrix deformation of the phyllite would need to be at the high strain rate end of naturally occurring deformation (10^{-10} to 10^{-8} s^{-1}) and/or the dislocation glide deformation field may need to be extended to lower temperatures.

The larger blocky domains most likely represent recovery after penetrative phyllite matrix deformation, the overall pyrite texture thus being a “core and mantle” or “mortar” structure. The pyrite grain represented by domains *v* and *ix* is an intergrowth; its spongy core may be out of the plane of section. Domain *i* is likely to be a

Fig. 7 Recrystallisation of spongy pyrite in specimen 215-21. **A** Plane-polarised reflected light image. **B** Forescatter orientation contrast image. Note that “euhedral” recrystallised pyrite is polydomainal and that the spongy core has a shape-preferred orientation. Symbols *i*-*x* relate upper hemisphere <100> pole figures to specific domains defined in the OC image. Domains are highlighted on the reflected light image for clarity. Pole figure *vii* relates to the spongy core domain. Summary rim <100> pole figure *x* picks out two common CPOs. <100> orientations highlighted by *three squares* are best developed in rim domains *iii*, *vi* and *viii* and core domain *vii*. <100> orientations highlighted by *three circles* are best developed in rim domains *v* and *ix*. Total number of orientations presented in the summary rim pole figure is greater than the sum of highlighted rim domains because it includes some analyses in the rim outwith those highlighted domains. Data and images collected using Philips XL30 SEM system

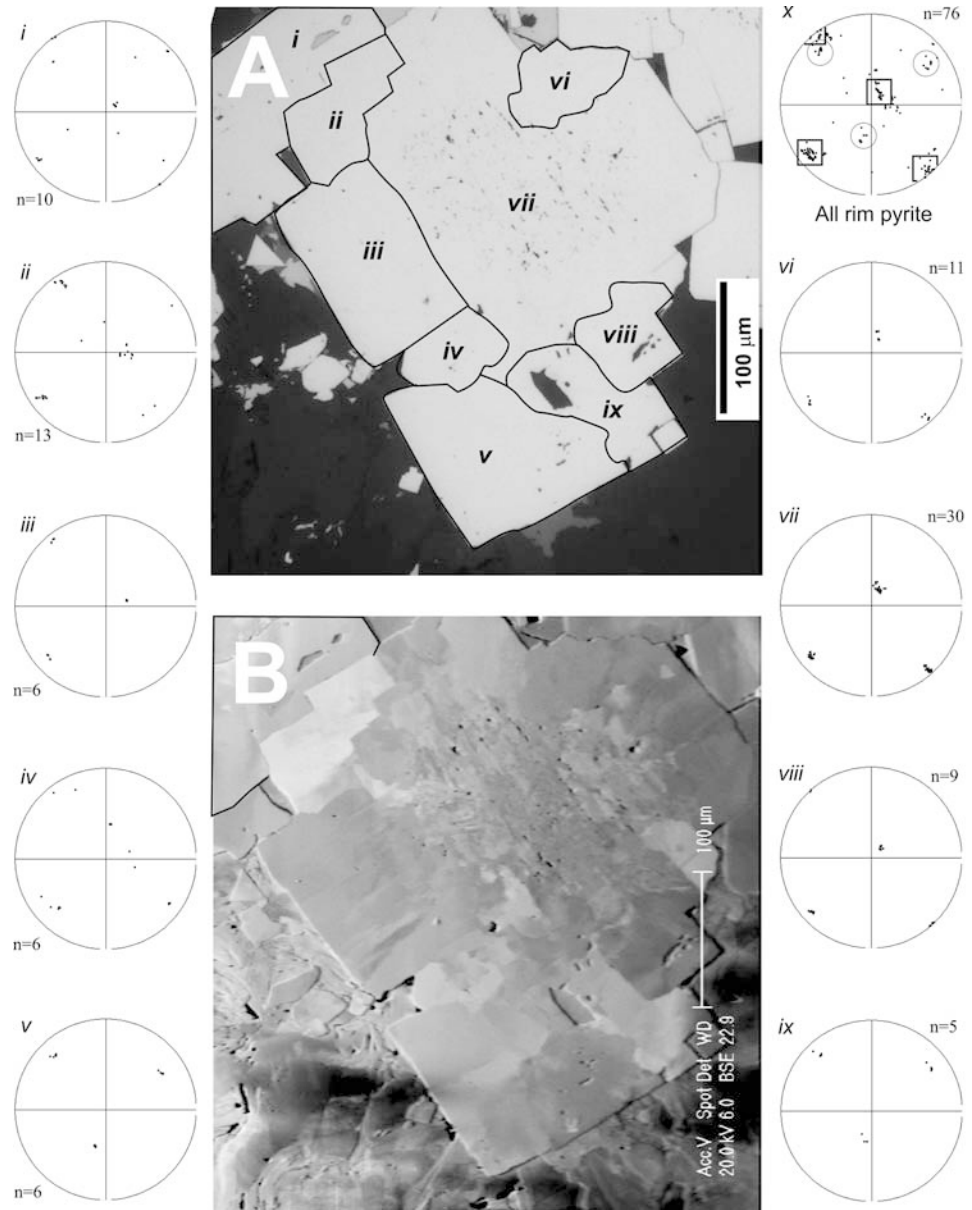
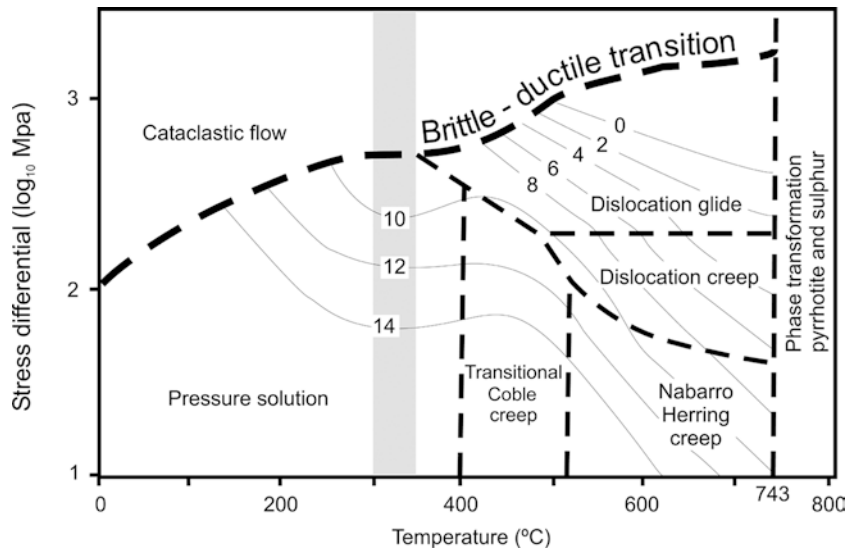


Fig. 8 Pyrite deformation mechanism map (McClay and Ellis 1983) for approx. 100-µm grain size. Contours for strain rate are labelled for 10^{-n} s^{-1} . Lower greenschist facies temperature conditions for Greens Creek, $325 \pm 25 \text{ }^\circ\text{C}$, are highlighted for reference



separate grain that happens to have a similar crystallographic orientation.

Specimen 224W5-38B pyrite blasts in sheared phyllite

Specimen 224W5-38B is from the West Bench ore body where the <5-m-thick ore horizon has been highly attenuated by strain during F_2 folding (Fig. 2). Within the sample, discrete higher strain zones developed. These are recognisable where sphalerite tails form shear-sense indicators on disseminated pyrite porphyroblasts (Fig. 9). In this example (Fig. 9A), the top-to-left shear sense indicated by the sphalerite tails would also indicate the potential for a reverse-sense of movement between the two larger pyrites featured. The pyrites are rather featureless in BSE image (Fig. 9A and B). Close examination of the contact between the two pyrites in OC image (Fig. 9C and D) reveals the presence of narrow, micron-scale, grey-scale bands together with some more block-shaped domains. The concentrically arranged bands in the right-hand pyrite are spatially located above a “ramp-like” feature in the left-hand pyrite, suggesting some genetic relationship. EBSD analysis of the concentric bands in the right-hand pyrite (Fig. 9) reveals a $\langle 100 \rangle$ pole figure pattern best explained as twist boundaries formed by screw dislocations mainly around one $\langle 100 \rangle$ axis (circled in Fig. 9). Each grey-scale band in image C represents an approximately 1° rotation, and these have a consistent sense resulting in a cumulative rotation of about 18° . The arrows show the rim-to-core lattice rotation sense. Cox (1987) attributes this type of lattice misorientation, which can be described by a rotation about an axis, to dislocation creep involving the development of twist boundaries by the knitting together of screw dislocations to form a network structure. In this example, $\{100\}$ represents the glide plane and $\langle 100 \rangle$ the rotation axis.

The lower grain shows a similar overall pole figure pattern with one $\langle 100 \rangle$ direction being effectively fixed (circled), while the other two disperse by approximately 20° with a consistent sense of rotation. However, the pattern is a little more complicated than for the top pyrite. In some domains, the rotation has taken place around the $\langle 100 \rangle$ direction labelled 2 in the pole figure. The blocky grey areas in Fig. 9C further illustrate this oscillatory switching between a main rotation axis and a minor rotation axis.

Sharply defined irregular boundaries between indented pyrites are typically interpreted as evidence for pressure solution (McClay and Ellis 1983), suggesting that pressure solution may have occurred between the two pyrites featured in Fig. 9. However, pressure solution cannot have been the dominant process. If it was, then the evidence for dislocation creep processes should not be so evident. Dislocation creep results from dislocation glide along $\{100\}$ planes, coupled with dislocation climb, and is normally associated with higher temperatures than implied by the Greens Creek metamorphic conditions (Fig. 8).

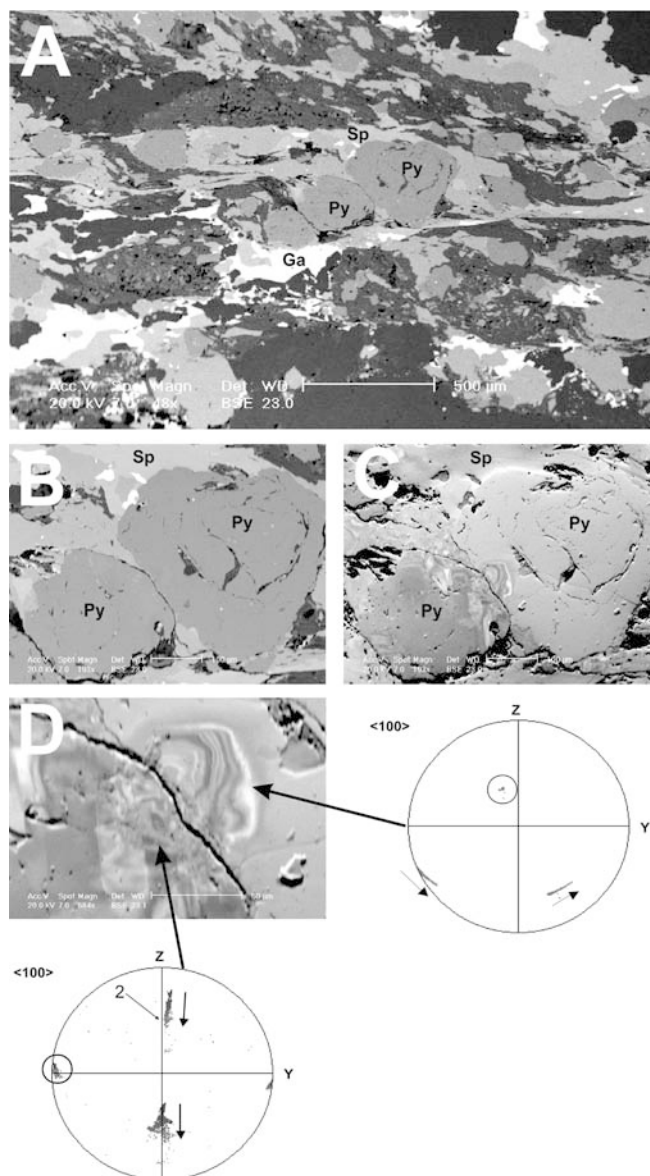


Fig. 9 Microfabrics in specimen 224W5-38B developed by dislocation glide. **A** is a backscatter-electron image showing asymmetric sphalerite strain shadows around pyrite, indicating a top to left sense of shear (*py* pyrite; *sp* sphalerite; *ga* galena). **B** and **C** are BSE and OC images, respectively, of two impinging pyrite blasts. Note that in the OC image (**C**), localised strain, resulting from variations in lattice orientation, can be seen. **D** illustrates misorientation bands in an OC image, defined by changes in grey scale that are localised around the ramp part of the suture between pyrite grains. Upper hemisphere pole figures for $\langle 100 \rangle$ axes indicate that deformation can be explained as twist boundaries formed by screw dislocations mainly around one $\langle 100 \rangle$ axis (circled). Arrows show rim-to-core lattice rotation sense for pyrite blasts. Images collected using Philips XL30 SEM system. EBSD data collected automatically on a micron-spaced grid basis using a CamScan X500 Crystal Probe SEM

One possibility is that the contact between the two pyrites in Fig. 9 localised strain, resulting in frictional heating and a localised higher temperature during the deformation. Alternatively, it may be that the dislocation creep field in Fig. 8 needs to move into lower temperature.

Discussion

This study has demonstrated that foreshatter orientation-contrast imaging coupled with electron backscatter diffraction provides a powerful set of tools for interpretation of pyrite textures. Complete answers may not be available, as yet, but it is clear that simple reliance on features seen in reflected light and/or SEM backscattered electron images is likely to be misleading, at best, for interpreting pyrite textures.

One future avenue of research that may prove fruitful is the coupling of EBSD with high-resolution chemical mapping. Trace element chemical variability within pyrite has been known for some time now (Craig et al. 1998), and studies in other minerals, such as olivine, are demonstrating linkages between deformation mechanisms (e.g. dislocation creep) and the microscale distribution of chemical elements (Ando et al. 2001). Application of high-resolution trace-element chemical mapping of the colloform and spongy textures may help resolve between primary-inherited (biogeochemical?) versus secondary-imposed (deformation/metamorphism) origins for their textures. It will also be of interest to investigate the possible link between internal plastic deformation of pyrite and trace element distributions.

McClay and Ellis's (1983) deformation mechanisms map for pyrite (Fig. 8) has been widely used. Cox (1987) suggested caution in using it, noting that where flow laws for pyrite have been experimentally determined, they have been done so for only a limited range of temperature, applied stress and strain rate (Cox et al. 1981; Graf et al. 1981; Levade et al. 1982). This study, like that of Boyle et al. (1998), suggests that the dislocation glide and creep fields may be better moved to lower temperatures and strain rates. In a wide-ranging review, Marshall and Gilligan (1987, Table 8) summarised deformation mechanisms in pyrite, thus:

“Cataclasis usually dominant to at least 450 °C, but pressure solution and grain boundary sliding can dominate behaviour in this range. Glide commences below 450 °C; dislocation flow with minor recovery between 450 °C and 550 °C; synkinematic recrystallisation important above 550 °C. Annealing and grain growth are significant at 550 °C+ in natural environments.”

They also suggested (Marshall and Gilligan 1987, Table 7) that the brittle-ductile transition was likely to be at about 450 °C at 300 MPa. This study suggests lower temperatures for the onset of glide and for the brittle-ductile transition. We suspect that more widespread application of the EBSD techniques described in this article to naturally occurring metamorphosed and deformed pyrite ores should help to improve our understanding of pyrite behaviour.

Acknowledgements We thank Kees Veldtkamp for assistance with SEM work, and Dave Prior for assistance with Channel+ and its related software programs at Liverpool University. We would like to thank Kennecott Greens Creek Mining Company for letting us study the samples and publish the results and Colorado School of

Mines for the travel grant that enabled Katja Freitag to visit Liverpool. Finally, the manuscript has benefited from careful reviews by Prof. Heinrich Siemes and Dr. Karen Kelley.

References

- Ando J, Shibata Y, Okajima Y, Kanagawa K, Furusho M, Tomioka N (2001) Striped iron zoning of olivine induced by dislocation creep in deformed peridotites. *Nature* 414:893–895
- Boyle AP, Prior DJ, Banham MH, Timms NE (1998) Plastic deformation of metamorphic pyrite: new evidence from electron-backscatter diffraction and foreshatter orientation-contrast imaging. *Miner Deposita* 34:71–81
- Brown D, McClay KR (1993) Deformation textures in pyrite from the Vangorda Pb-Zn-Ag deposit, Yukon, Canada. *Min Mag* 57:55–66
- Castroviejo R (1990) Gold ores related to shear zones, west Santa Comba–Fervenza area (Galicia, NW Spain)—a mineralogical study. *Miner Deposita* 25:S42–S52
- Cox SF (1987) Flow mechanisms in sulphide minerals. *Ore Geol Rev* 2:133–171
- Cox SF, Etheridge MA, Hobbs BE (1981) The experimental ductile deformation of polycrystalline and single-crystal pyrite. *Econ Geol* 76:2105–2117
- Craig JR, Vokes FM (1993) The metamorphism of pyrite and pyritic ores—an overview. *Min Mag* 57:3–18
- Craig JR, Vokes FM, Solberg TN (1998) Pyrite: physical and chemical textures. *Miner Deposita* 38:82–101
- Freitag K (2000) Geology and structure of the Lower Southwest orebody, Greens Creek mine, Alaska. Colorado School of Mines, Colorado, USA
- Gaspar O, Pinto A (1991) The ore textures of the Neves-Corvo volcanogenic massive sulfides and their implications for ore beneficiation. *Min Mag* 55:417
- Graf JL, Skinner BJ, Bras J, Fagot M, Levade C, Couderc JJ (1981) Transmission electron-microscopic observation of plastic-deformation in experimentally deformed pyrite. *Econ Geol* 76:738–742
- Himmelberg GR, Brew DA, Ford AB (1994) Petrologic characterization of pelitic schists in the western metamorphic belt, coast plutonic-metamorphic complex, near Juneau, southeastern Alaska. *US Geol Surv Bull* 2074:18
- Himmelberg GR, Brew DA, Ford AB (1995) Low-grade, M1 metamorphism of the Douglas Island volcanics, western metamorphic belt near Juneau, Alaska. In: Schiffman P, Day HW (eds) Low-grade metamorphism of mafic rocks. *Geol Soc Am Spec Pap* 296:51–66
- Levade C, Couderc JJ, Bras J, Fagot M (1982) Transmission electron-microscopy study of experimentally deformed pyrite. *Philos Mag A Defects Mech Prop* 46:307–325
- Marshall B, Gilligan LB (1987) An introduction to remobilization: information from ore-body geometry and experimental considerations. *Ore Geol Rev* 2:87–131
- McClay KR, Ellis PG (1983) Deformation and recrystallization of pyrite. *Min Mag* 47:527–538
- Ohfuji H, Akai J (2002) Icosahedral domain structure of framboidal pyrite. *Am Mineral* 87:176–180
- Ohfuji H, Akai J, Butler I, Rickard D (2002) Icosahedral domain structure of framboidal pyrite and its significance on the framboid formation. In: Parsons I (ed) *Mineralogy for the new millennium: programme with abstracts*. Mineralogical Society of Great Britain and Ireland, Edinburgh, 112 pp
- Prior DJ, Trimby PW, Weber UD, Dingley DJ (1996) Orientation contrast imaging of microstructures in rocks using foreshatter detectors in the scanning electron microscope. *Min Mag* 60:859–869
- Prior DJ, Boyle AP, Brenker F, Cheadle MC, Day A, Lopez G, Potts GJ, Reddy SM, Spiess R, Trimby PW, Wheeler J, Zetterström L (1999) The application of electron backscatter

- diffraction and orientation contrast imaging in the SEM to textural problems in rocks. *Am Mineral* 84:1741–1759
- Prior DJ, Wheeler J, Peruzzo L, Spiess R, Storey C (2002) Some garnet microstructures: an illustration of the potential of orientation maps and misorientation analysis in microstructural studies. *J Struct Geol* 24:999–1011
- Siemes H, Zilles D, Cox SF, Merz P, Schafer W, Will G, Schaeben H, Kunze K (1993) Preferred orientation of experimentally deformed pyrite measured by means of neutron diffraction. *Min Mag* 57:29–43
- Spiess R, Peruzzo L, Prior DJ, Wheeler J (2001) Development of garnet porphyroblasts by multiple nucleation, coalescence and boundary misorientation driven rotations. *J Metamorphic Geol* 19:269–290
- Taylor CD, Newkirk SR, Hall TE, Lear KG, Premo WR, Leventhal JS, Meier AL, Johnson CA, Harris AG (1999) The Greens Creek deposit, southeastern Alaska: A VMS-SEDEX hybrid. In: Stanley CJ (eds) *Mineral deposits: processes to processing*. AA Balkema, Rotterdam, pp 597–600
- Taylor CD, Premo WR, Lear KG (2000) The Greens Creek massive sulfide deposit; premier example of the Late Triassic metallogeny of the Alexander Terrane, southeastern Alaska and British Columbia. In: *Proc Geological Society of America, Cordilleran Section, 96th Annu Meeting (Abstr with Programs)* 32:71
- Wilkin RT, Barnes HL, Brantley SL (1996) The size distribution of framboidal pyrite in modern sediments: an indicator for redox conditions. *Geochim Cosmochim Acta* 60:3897–3912
- Xu G (1996) Structural geology of the Dugald River Zn-Pb-Ag deposit, Mount Isa Inlier, Australia. *Ore Geol Rev* 11:339–361